Draft version February 4, 2014
Preprint typeset using LaTeX style emulateapj v. 5/2/11

arXiv:1401.8001v2 [astro-ph.GA] 3 Feb 2014

MIXING IN MAGNETIZED TURBULENT MEDIA

Sharanya Sur[1], Liubin Pan[2] & Evan Scannapieco[1]

Draft version February 4, 2014

ABSTRACT

Turbulent motions are essential to the mixing of entrained fluids and are also capable of amplifying weak initial magnetic fields by small-scale dynamo action. Here we perform a systematic study of turbulent mixing in magnetized media, using three-dimensional magnetohydrodynamic simulations that include a scalar concentration field. We focus on how mixing depends on the magnetic Prandtl number, Pm, from 1 to 4 and the Mach number, $\mathcal{M}$, from 0.3 to 2.4. For all subsonic flows, we find that the velocity power spectrum has a $k^{-5/3}$ slope in the early, kinematic phase, but steepens due to magnetic back reactions as the field saturates. The scalar power spectrum, on the other hand, flattens compared to $k^{-5/3}$ at late times, consistent with the Obukohov-Corrsin picture of mixing as a cascade process. At higher Mach numbers, the velocity power spectrum also steepens due to the presence of shocks, and the scalar power spectrum again flattens accordingly. Scalar structures are more intermittent than velocity structures in subsonic turbulence while for supersonic turbulence, velocity structures appear more intermittent than the scalars only in the kinematic phase. Independent of the Mach number of the flow, scalar structures are arranged in sheets in both the kinematic and saturated phases of the magnetic field evolution. For subsonic turbulence, scalar dissipation is hindered in the strong magnetic field regions, probably due to Lorentz forces suppressing the buildup of scalar gradients, while for supersonic turbulence, scalar dissipation increases monotonically with increasing magnetic field strength. At all Mach numbers, mixing is significantly slowed by the presence of dynamically-important small-scale magnetic fields, implying that mixing in the interstellar medium and in galaxy clusters is less efficient than modeled in hydrodynamic simulations.

Subject headings: turbulence, magnetic fields, MHD, ISM: abundances

1. INTRODUCTION

Turbulent mixing is an important topic with many applications (Dimotakis 2005), from atmospheric research (e.g., Jacobson 2001), to combustion (e.g., Pitsch 2006), to astrophysics. Within and around our galaxy, for example, mixing in turbulent flows is essential to interpret a wide variety observations including the metallicity dispersion in open clusters (Friel & Boesgaard 1992; Quillen 2002; De Silva et al. 2006), the abundance of scatter along different lines of sight in the interstellar medium (ISM) Cartledge et al. (2006), and the cluster to cluster metallicity scatter (Twarog et al. 1997). At moderate redshifts, mixing is a key process in the enrichment of the intergalactic medium (e.g, Schaye et al. 2003; Pichon et al. 2003; Pieri et al. 2006; Scannapieco et al. 2006; Becker et al. 2009) and the distribution of metals in galaxy clusters (Rebusco et al. 2005; David & Nulsen 2008; Brüggen & Scannapieco 2009). At the highest redshifts, mixing determines the pollution of primordial gas by the first generation of stars in early galaxies (Pan & Scalo 2007; Pan et al. 2011, 2013) and the transition from Population III to Population II star formation (Scannapieco et al. 2003).

Over the course of the last decades, advances in numerical modeling of turbulent flows have broadened our understanding of turbulent mixing. This has led to a confirmation of the physical picture of turbulent mixing, often referred to as the 'Obukohov-Corrsin' (OC) phenomenology (Shraiman & Siggia 2000) in which scalar mixing is described as a cascade process caused by the stretching of the concentration field by the velocity field. The scalar field advected by the turbulent flow thus exhibits a complex, chaotically evolving structure over a broad range of spatial and temporal scales. Random stretching by the velocity field leads to the production of scalar structures of progressively smaller size, down to the scale at which molecular diffusion eventually homogenizes the scalar fluctuations. This description has so far been also confirmed numerically for both incompressible and compressible hydrodynamic turbulence (Shraiman & Siggia 2000; Pan & Scannapieco 2010, 2011; Pan et al. 2013).

The turbulent motions responsible for mixing also amplify and maintain magnetic fields in astrophysical systems by the dynamo mechanism wherein kinetic energy in turbulent fluid motions is tapped to amplify the mag-

sharanya.sur@asu.edu, lpan@cfa.harvard.edu, evan.scannapieco@asu.edu
[1] School of Earth and Space Exploration, Arizona State University, PO Box 876004, Tempe - 85287, USA
[2] Harvard-Smithsonian Center for Astrophysics, 60 Garden St., Cambridge MA 02138, USA

netic energy (see Brandenburg et al. 2012, for a review). The basic underlying mechanism responsible for this dynamo action is the random stretching and folding of the field lines by the turbulent eddies. This leads to initial exponential amplification of the magnetic field, followed by an intermediate stage of linear growth as fields on progressively larger scales reach dynamically important strengths, and finally by a saturated phase as fields on all length scales become large enough to resist further stretching.

There are two main types of astrophysical dynamos. Large-scale dynamos generate magnetic fields on scales larger than the energy-carrying scale of turbulence, whereas small-scale dynamos generate magnetic fields on scales comparable to the scale of turbulence. While large-scale magnetic fields require special conditions like the presence of helical turbulence (Krause & Raedler 1980; Ruzmaikin et al. 1988), small-scale dynamos are generic in any random turbulent flow in which the magnetic Reynolds number Rm, exceeds a critical value $\mathrm{R_{cr}} \approx 35 - 100$ (Brandenburg & Subramanian 2005). Such dynamos are capable of amplifying fields on the eddy turnover time scale, which is much shorter than the overall age for many astrophysical systems, including galaxies and galaxy clusters. This implies that the small-scale dynamo will be crucial for magnetic field generation in many astrophysical objects including systems in which conditions for large-scale dynamo operation is unlikely. For example, recent high-resolution numerical simulations have also hinted at the possible presence of magnetic fields in the first stars (Sur et al. 2010; Federrath et al. 2011b; Turk et al. 2012; Bromm 2013; Glover 2013; Latif et al. 2013), amplified by small-scale dynamo action from seed fields obtained by the Biermann battery mechanism (Biermann 1950) in the early Universe.

Given the omnipresent nature of astrophysical magnetic fields, it is important to study how mixing occurs in a magnetized medium in which the small-scale dynamo is operating. As both mixing and the small-scale dynamo are driven by turbulence, this situation will arise naturally in astrophysical systems as diverse as the metal-rich interstellar medium (de Avillez & Mac Low 2002), the inhomogeneously-enriched intracluster medium within galaxy clusters, (Ruszkowski & Oh 2010; Sakuma et al. 2011; Churazov et al. 2012), and the gas collapsing onto the very first galaxies, into which metals are being mixed for the first time (Pan et al. 2013). Here, we address this issue using non-ideal magnetohydrodynamic (MHD) numerical simulations in which turbulence is randomly forced in the presence of initially weak magnetic fields. Furthermore, we characterize pollutants such as metals as a scalar field satisfying the advection-diffusion equation and allow for continuous injection of pollutants on the driving scale of turbulence.

The structure of the paper is as follows. In Section 2, we describe the numerical method and the simulation setup used in our study. The results are presented in Section 3, where we discuss the time evolution our simulations, present a qualitative and quantitative discussion of the structure of the density, velocity, magnetic and the scalar concentration fields, and evaluate the impact of the small-scale dynamo on the overall mixing timescale. A summary of our results and conclusions is given in Section 4.

2. NUMERICAL METHOD AND INITIAL CONDITIONS

To study turbulent mixing in the presence of evolving magnetic fields, we simulated continuously-driven, three-dimensional turbulence in a periodic box with an initially weak magnetic field using the Eulerian grid code FLASHv4[3] (Fryxell et al. 2000). We solved the full set of non-ideal MHD equations given below on a uniform grid with a resolution of 512^3 points for a domain of unit size with periodic boundary conditions.

$$\partial_t \rho + \nabla \cdot (\rho \mathbf{u}) = 0, \tag{1}$$

$$\rho \left[\partial_t \mathbf{u} + (\mathbf{u}\cdot\nabla)\mathbf{u}\right] = (\mathbf{B}\cdot\nabla)\mathbf{B} - \nabla p' + \nabla\cdot(2\nu\rho\boldsymbol{\mathcal{S}}) + \rho\mathbf{F}, \tag{2}$$

$$\partial_t E + \nabla\cdot[E\mathbf{u}] = -\nabla\cdot(p'\mathbf{u}) + \nabla\cdot[(\mathbf{B}\cdot\mathbf{u})\,\mathbf{B}] + \nabla\cdot[\mathbf{B}\times(\eta\nabla\times\mathbf{B}) + 2\nu\rho\mathbf{u}\cdot\boldsymbol{\mathcal{S}}], \tag{3}$$

$$\partial_t \mathbf{B} + (\mathbf{u}\cdot\nabla)\mathbf{B} = (\mathbf{B}\cdot\nabla)\mathbf{u} - \mathbf{B}(\nabla\cdot\mathbf{u}) + \eta\nabla^2\mathbf{B}, \tag{4}$$

$$\nabla\cdot\mathbf{B} = 0, \tag{5}$$

where ρ, $\mathbf{u}$, $p' = p + \frac{1}{2}|\mathbf{B}|^2$, $\mathbf{B}$, and $E = \rho\epsilon_{\rm int} + \frac{1}{2}\rho|\mathbf{u}|^2 + \frac{1}{2}|\mathbf{B}|^2$ denote density, velocity, pressure (thermal and magnetic), magnetic field, and total energy density (internal, kinetic, and magnetic). The first term on the right hand side of eq. (2) accounts for the magnetic tension due to Lorentz forces, and the other component of the Lorentz force, the magnetic pressure, is included in the second term. In this equation, the last term is the artificial driving term for turbulence, and viscous and resistive interactions are included in eqs. (3-5) via the traceless rate of strain tensor, $\mathcal{S}_{ij} = (1/2)(\partial_i u_j + \partial_j u_i) - (1/3)\delta_{ij}\partial_k u_k$, and ν and η are the kinematic viscosity and the magnetic resistivity respectively. The first term on the right hand side in eq. (3) is the pdV work in the presence of magnetic fields while the second term corresponds to a component derived from the Lorentz force. The stretching of the magnetic field lines by a turbulent flow corresponds to the first term on the right hand side of eqn. (4), while the second term denotes compression of the field lines. The last term accounts for magnetic field dissipation. Our simulations employed the unsplit staggered mesh algorithm in FLASHv4 with a constrained transport scheme to maintain $\nabla\cdot\boldsymbol{B} = 0$ to machine precision (Lee & Deane 2009; Lee 2013) and the HLLD Riemann solver (Miyoshi & Kusano 2005).

In addition to these equations, pollutants are characterized as a scalar field, C, which obeys the advection-

[3] http://flash.uchicago.edu/site/flashcode/

diffusion equation

$$\partial_t (\rho C) + \nabla \cdot [\rho C \mathbf{u} - \rho\kappa \nabla C] = \rho \mathbf{T}, \quad (6)$$

where κ is the scalar diffusion coefficient and $\mathbf{T}$ is the random forcing term for driving the scalars. We included these scalar diffusion and forcing terms in a separate module in FLASHv4. As described in detail in Pan & Scannapieco (2010), an equation for the evolution of density-weighted variance can be derived from eq. (6) with the help of the continuity equation, yielding

$$\partial_t \langle \tilde{\rho} C^2 \rangle + \partial_i \langle \tilde{\rho} C^2 u_i \rangle = 2\langle \partial_i (\tilde{\rho}\kappa C \partial_i C) \rangle - 2\langle \tilde{\rho}\kappa (\partial_i C)^2 \rangle + 2\langle \tilde{\rho} T C \rangle. \quad (7)$$

where the density-weighting factor $\tilde{\rho}$ is the ratio of ρ to the average flow density, $\bar{\rho}$, in the flow, and $\langle \cdots \rangle$ denotes an ensemble average, which is equal to the average over the flow domain for statistically homogeneous flows, as in our simulations.

The second term on the left hand side of this equation is an advection term, which corresponds to the spatial transport of concentration fluctuations between different regions. In the statistically homogeneous case, as in our simulations, this term vanishes, and in its absence, eq. (7) does not have an explicit dependence on the velocity field. This implies that the velocity field does not truly mix. In fact, this also holds true in an inhomogeneous flow. While the advection term is non-zero in this case, it is a surface term, and thus its integral over the entire flow domain is zero, which means that advection conserves the global scalar variance.

The first two terms on the right hand side of the above equation originate from the scalar diffusion term in eq. (6). The first of these again vanishes in the homogeneous case and leads to a conservation of the global scalar variance in the inhomogeneous case. The term $\bar{\epsilon}_{\rm c} \equiv -2\langle \tilde{\rho}\kappa (\partial_i C)^2 \rangle$ represents the scalar dissipation rate. The linear dependence on κ in the expression for $\bar{\epsilon}_{\rm c}$ may imply a strong dependence of the scalar dissipation rate on κ. However, this is not true because the scalar gradient also depends on κ. With decreasing κ, larger scalar gradients can develop, which may compensate the decrease in κ, as we shall see below. The last term on the right hand side of eq. (7) is the source term, which corresponds to the increase in scalar variance due to the injection of new pollutants.

To drive turbulence, we used an artificial forcing term $\mathbf{F}$ in the momentum equation (see eqn. 2) which is modeled as a stochastic Ornstein-Uhlenbeck (OU) process (Eswaran & Pope 1988; Benzi et al. 2008) with a user-specified forcing correlation time t_f. For all simulations reported here, we drove turbulence with solenoidal forcing (i.e., $\nabla \cdot \mathbf{F} = 0$) in the range of wavenumbers, $1 \leq |\mathbf{k}| L/2\pi \leq 3$ such that the average forcing wavenumber is $k_{\rm f}\, L/2\pi \simeq 2$. The driving scheme can thus be summarized as $\langle F_i(\mathbf{k}, t)\, F_j(\mathbf{k}, t') \rangle = \mathcal{P}_{\rm f}(k) \left(\delta_{ij} - k_i k_j / k^2\right) \exp[-(t - t')/t_f]$. Our choice of solenoidal forcing is motivated by the fact that the dynamo is more efficient for solenoidal driving compared to turbulence driven purely by compressive forcing due to more pronounced shearing motions in the former case. In reality though, turbulence is expected to be of mixed type consisting of both solenoidal and compressive motions.

The random forcing for the scalar field $\mathbf{T}$ is identical to the velocity forcing, $\langle T(\mathbf{k}, t)\, T(\mathbf{k}, t') \rangle = \mathcal{P}_{\rm T}(k) \exp[-(t - t')/t_s]$ with $\mathcal{P}_T(k) \propto \mathcal{P}_F(k)$ and t_s is the scalar correlation time. In other words, pollutants are continuously injected in our simulations on scales equal to the driving scale of the flow. This is similar in spirit to the actual scenario in the ISM where, for mixing of new metals from supernovae (SNe), the source length scale is the same as the driving scale of turbulence. On the other hand, if we consider self-enrichment in star-forming clouds, the two scales could be different as the driving scale of turbulent energy is mainly from the cascade of the interstellar turbulence on scales much larger than the scalar source scale which could be within the star-forming cloud (e.g., Pan et al. 2012). We refer the reader to Pan & Scannapieco (2010) for a detailed analysis of the dependence of turbulent mixing depending on scalar source size.

In all our runs, we adopted an isothermal equation of state and an initial density and sound speed set to unity. The initial magnetic field, $B_0 = (0, 0, B_{0z})$ was in the z-direction with a plasma beta, defined as the ratio of the thermal and magnetic pressures, varied between $\beta = 2p/B^2 = 10^4 - 10^7$. These values of β allowed us to explore the problem at hand within a reasonable computational time. Similar to Pan & Scannapieco (2010), we chose the forcing correlation time for both t_f ans t_s to be $1/2$ the sound crossing timescale, defined as the box size divided by the sound speed. This approach ensures that the forcing correlation time is constant for each simulation[4].

Also similar to the study of Pan & Scannapieco (2010), we used three independent scalars, each of which had the same source spectrum, which also matched the spectrum of the velocity forcing. This approach ensures smaller temporal variations in the scalar variance compared to the temporal variations of the rms value of the concentration of each individual scalar. Moreover, we chose the scalar source term to have a zero mean and therefore did not consider the evolution of the mean concentration in our simulations[5]. The negative concentration values in

[4] The choice of an appropriate forcing correlation may depend on the problem of interest. In some cases, numerical studies of small-scale dynamos employ a delta-correlated forcing as in Haugen et al. (2004). This choice is a simplified choice which may not apply for realistic astrophysical flows. However, since the amplification of the magnetic field is driven by eddies below the driving scale, the properties of the small-scale dynamo can be expected to have only a minor dependence on the large-scale driving pattern. In fact, the small-scale dynamo has also been obtained for a finite time forcing correlation (Cho et al. 2009; Federrath et al. 2011a). In the context of scalar mixing, Pan & Scannapieco (2010) verified that different choices of the forcing correlation did not affect the scalar statistics.

[5] Using a Gaussian source term is a common practice in the the-

our simulation are to be understood as relative to the mean concentration. In this sense, the negative values of the scalar concentration in our simulations should be interpreted as under-enriched regions in the simulation volume. Thus the addition of large scale regions with negative scalar concentration could correspond to an inflow of intergalactic gas onto a galaxy or the collapse of additional interstellar gas onto a self-enriched molecular cloud.

All our simulations were performed with a Schmidt number, $\mathrm{Sc} = \mathrm{Pe}/\mathrm{Re} = \nu/\kappa = 1$ with constant kinematic viscosity and scalar diffusivity. Here Pe and Re are the Peclet and the fluid Reynolds number respectively. In order to explore the parameter space, we adopted a two-fold simulation strategy. First, we explored turbulent mixing as a function of the rms Mach number ($\mathcal{M}_{\rm rms} \approx 0.3, 1.1, 2.3$) for a constant Prandtl number of unity (i.e., $\mathrm{Pm} = \mathrm{Rm}/\mathrm{Re} = \nu/\eta = 1$) at $\mathrm{Re} = \mathrm{Rm} \approx 1250$. Here $\mathrm{Rm} = u\, l_{\rm f}/\eta$ is the magnetic Reynolds number with u being the rms velocity and $l_{\rm f} = 2\pi/k_{\rm f}$ the driving scale of turbulence. Next, we explored the mixing of pollutants as a function of the Prandtl number for a fixed Mach number. To this end, we conducted simulations at $\mathrm{Pm} = 1, 2$ and 4 for a subsonic rms $\mathcal{M} = 0.3$. To achieve $\mathrm{Pm} > 1$, we increased the kinematic viscosity ν (thereby decreasing Re) instead of decreasing the magnetic diffusivity η so as to ensure that most of the scales of the velocity and the magnetic field remained resolved at 512^3 resolution. Furthermore, this approach helps us to probe if there are qualitative differences in the turbulent mixing depending on whether the flow field is turbulent or random. In addition, we also conducted two ideal MHD simulations at $\mathcal{M} = 0.3$ with initial plasma beta $\beta_{\rm in} = 10^4$ and 10^7 respectively and another ideal run at $\mathcal{M} = 2.4$ with $\beta_{\rm in} = 10^7$. In these runs, the viscous and the diffusive scales are determined by the numerical scheme rather than the user, although larger inertial ranges are achieved. In all cases, the magnetic Reynolds number $\mathrm{Rm} > \mathrm{R_{cr}}$ ensuring magnetic field growth by dynamo action. Table 1 provides a summary of the simulation runs we performed.

Simulation Run	Init. Plasma Beta, $\beta_{\rm in}$	Rms Mach $\mathcal{M}_{\rm rms}$	Prandtl # $\mathrm{Pm} = \mathrm{Rm}/\mathrm{Re}$	Reynolds # $\mathrm{Re} = u\, l_f/\nu$
M0.3Pm1a	10^4	≈ 0.3	1	≈ 1250
M0.3Pm1b	10^7	≈ 0.3	1	≈ 1250
M0.3Pm2	10^4	≈ 0.3	2	≈ 620
M0.3Pm4	10^4	≈ 0.3	4	≈ 312
M1.1Pm1	10^4	≈ 1.1	1	≈ 1250
M2.3Pm1	10^4	≈ 2.3	1	≈ 1400
M0.3Id1	10^4	≈ 0.3	$\approx O(1)$	——
M0.3Id2	10^7	≈ 0.3	$\approx O(1)$	——
M2.4Id	10^7	≈ 2.4	$\approx O(1)$	——

Table 1
Summary of the simulation runs presented in this paper at a uniform grid resolution of 512^3. The non-ideal MHD runs are classified as M**X**Pm**Y** where **X** refers to the value of the Mach number and **Y** refers to the value of Prandtl number. M2.3Pm1 is only followed up to the linear growth phase. M0.3Id1 and M0.3Id2 are the two ideal MHD runs at $\mathcal{M} = 0.3$ with $\beta_{\rm in} = 10^4$ and 10^7 respectively. M2.4Id corresponds to an ideal run at $\mathcal{M} = 2.4$ with $\beta_{\rm in} = 10^7$. In all the runs, the Schmidt number $\mathrm{Sc} = \nu/\kappa = 1$.

3. RESULTS

3.1. *Time Evolution*

The general properties of the small-scale dynamo have been extensively studied with the help of direct numerical simulations (Schekochihin et al. 2002, 2004; Haugen et al. 2004; Brandenburg & Subramanian 2005; Cho et al. 2009; Cho & Ryu 2009; Federrath et al. 2011a; Brandenburg et al. 2012; Beresnyak 2012; Bhat & Subramanian 2013, and other references therein) for both incompressible and compressible turbulence. The magnetic field is amplified by random stretching and folding by the turbulent eddies. This occurs exponentially at first, in what is labeled the kinematic phase, with the magnetic energy peaking on scales nearer to or somewhat larger than the dissipation scale. Once energy equipartition is attained on these scales, the stretching of the magnetic field lines is hindered by the magnetic back reaction and an intermediate stage of linear growth follows. At this stage, the peak of the magnetic power spectrum begins to shift as the magnetic field attains equipartition on increasingly larger scales. Eventually, when the magnetic energy density becomes comparable to the kinetic energy density close to the driving scale of turbulence, field amplification by the small-scale dynamo becomes impossible, and the system enters the saturated phase.

Our main objective here is to explore how the mixing of pollutants evolve as the magnetic field builds up due to small-scale dynamo action. In the kinematic phase we expect the mixing to be similar to that of a hydrodynamical simulation as the magnetic field is dynamically unimportant. To explore this, we conduct an ideal and a non-ideal run at $\mathcal{M} = 0.3$ and an ideal run at $\mathcal{M} = 2.4$ with $\beta_{\rm in} = 10^7$, which allow for a kinematic growth phase sufficient for our purpose. However, to break new ground, it is more important to investigate the effect of the magnetic field on the scalar mixing in the regime in which the magnetic field becomes dynamically important to back react on the flow, as will occur in any continuously enriched and driven magnetized turbulent medium. Therefore, we conduct most of our simulations with $\beta_{\rm in} = 10^4$, sacrificing the majority of the kinematic regime in favor of probing the mixing properties in the saturated phase within reasonable computational time and resources.

Figure 1 shows the evolution of the kinetic and magnetic energies and the rms value of the scalar concentration field as a function of the eddy turnover time $t_{\rm ed} = l_{\rm f}/u_{\rm rms}$. The presence of a very short kinematic phase does not allow us to make statements about the growth rate of the magnetic field. Nevertheless, in the

oretical studies of passive scalars physics, as it isolates the mixing physics from the possible complexities arising from the pollutant sources.

range $t = (1 - 2.5)\, t_{\rm ed}$, panel 1(b) shows the decrease in growth rate with increasing Mach number. The inset figure in panel 1(b) shows more clearly the diminishing growth rate of the magnetic field as the Mach number increases from $\mathcal{M} = 0.3$ to 2.4 for the ideal runs, which start from an initial $\beta = 10^7$. For solenoidal forcing, such a decrease in growth rate as the turbulent flow becomes supersonic has been previously reported in direct simulations of the small-scale dynamo (Federrath et al. 2011a). However, they also claimed the growth rate starts to increase for $\mathcal{M} > 2.4$, which we do not address here.

In our simulations, the growth rate also seems to decrease with increasing Pm (and decreasing Re and Pe), although a more extended kinematic range is required to settle this issue. The transition to the intermediate stage of magnetic field growth at the end of the kinematic phase is clearly seen for $\mathcal{M} = 1.1$ where it extends from $t \approx (4 - 10)\, t_{\rm ed}$, while for $\mathcal{M} = 2.4$, the intermediate growth phase is $t \approx (10 - 20)\, t_{\rm ed}$. The magnetic field finally saturates at a level depending on the Mach number of the flow. We note here that the high Mach number runs are typically more expensive than their subsonic counterparts. This is mainly due to two reasons. First, the resulting time step becomes smaller from subsonic to supersonic due to the Courant-Friedrichs-Lewy (CFL) condition and secondly, the presence of supersonic motions means that a substantial fraction of the kinetic energy is contained in shocks, which are relatively inefficient at driving the dynamo. This leads to a reduced growth rate of the magnetic field. In panel 1(c), we plot the time evolution of the rms value of the scalar concentration field for the above runs. The evolution of the rms value of the scalar concentration shows that $C_{\rm rms}$ increases as the flow moves from the kinematic phase to the saturated phase. Furthermore, in both the kinematic and saturated phases, $C_{\rm rms}$, increases with increasing Mach number, but is largely independent of Pm.

3.2. *Overall Field Structure*

In Fig. 2 we show three-dimensional volume renderings of the density, magnetic field, and the scalar concentration field for both the ideal and the non-ideal $\mathcal{M} = 0.3$ runs at $t \approx 2.5 t_{\rm ed}$, corresponding to the kinematic phase when the magnetic field is too weak to affect the flow. Fig. 3, shows similar renderings of the same fields at $t \approx 8.8 t_{\rm ed}$ corresponding to the saturated state when nonlinear back reactions resist further stretching and folding of the field by the turbulent eddies.

Several qualitative differences are apparent in these plots. In the non-ideal MHD run, magnetic and scalar structures are thick compared to the ideal MHD run, due to the inclusion of explicit resistivity and diffusion. As explained in the previous section, we start with a weak vertical magnetic field that then gets randomly stretched and folded as the turbulence is stirred in the box. In the kinetic phase, the magnetic field is like white noise, and from panels 2a and 2b in Fig. 2, we see that it appears to have strong positive/negative values (denoted by yellow/blue) in only a few regions in the simulation volume where random stretching by turbulent eddies is efficient in growing the field. At late times, on the other hand, the coherence length of the magnetic field grows to near the driving scale, saturating in a configuration shown in panels 2a and b in Fig. 3.

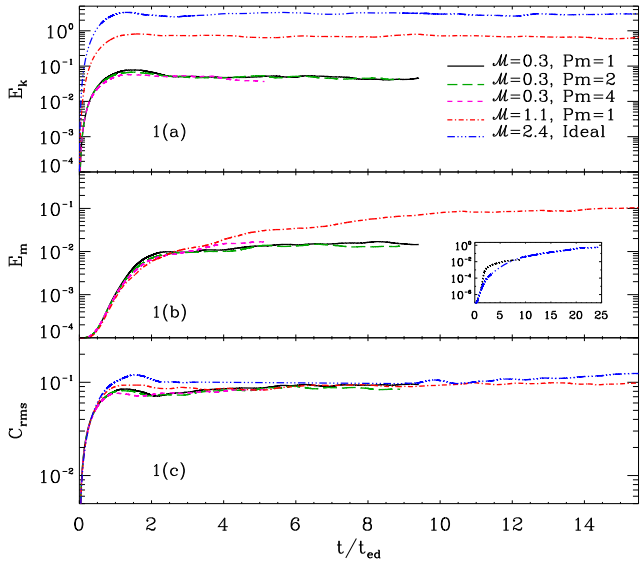

Figure 1. Time evolution of the kinetic energy (panel 1a), magnetic energy (panel 1b), and the rms value of the scalar concentration (panel 1c) for the different MHD runs starting with $\beta_{\rm in} = 10^4$ and 10^7. The inset figure in panel 1(b) shows the growth of the magnetic energy for M0.3Id2 (black, dotted) and M2.4Id (blue, dash-dotted) runs.

Similar to the magnetic field, the scalar field also shows numerous small-scale structures with sharp concentration contrasts in the kinematic phase resulting from random stretching and shearing by turbulent eddies (clearly visible in panel 3a in Fig. 2). Such sharp contrasts, unlike shocks, are not discontinuous, but rather have a small, but significant thickness. They are usually referred to as 'cliffs and ramps' in incompressible passive scalar turbulence (Sreenivasan 1996; Shraiman & Siggia 2000). They are produced by turbulent stretching, which amplifies scalar gradients by bringing fluid elements with very different concentration levels next to each other. As the magnetic field saturates, the morphology of the scalar structures changes to long ribbon-like filaments as shown in panels 3a and 3b in Fig. 3. This appears to be an effect of the magnetic field and was not seen previously in the hydrodynamical simulations of Pan & Scannapieco (2010). A quantitative analysis of the properties of the scalar structures is presented in the next subsection.

3.3. *Power Spectra and Structure Functions*

3.3.1. *Power Spectra*

In Figure 4, we plot the three-dimensional power spectra of the velocity, magnetic and the scalar concentration field for the different runs, in both the kinematic

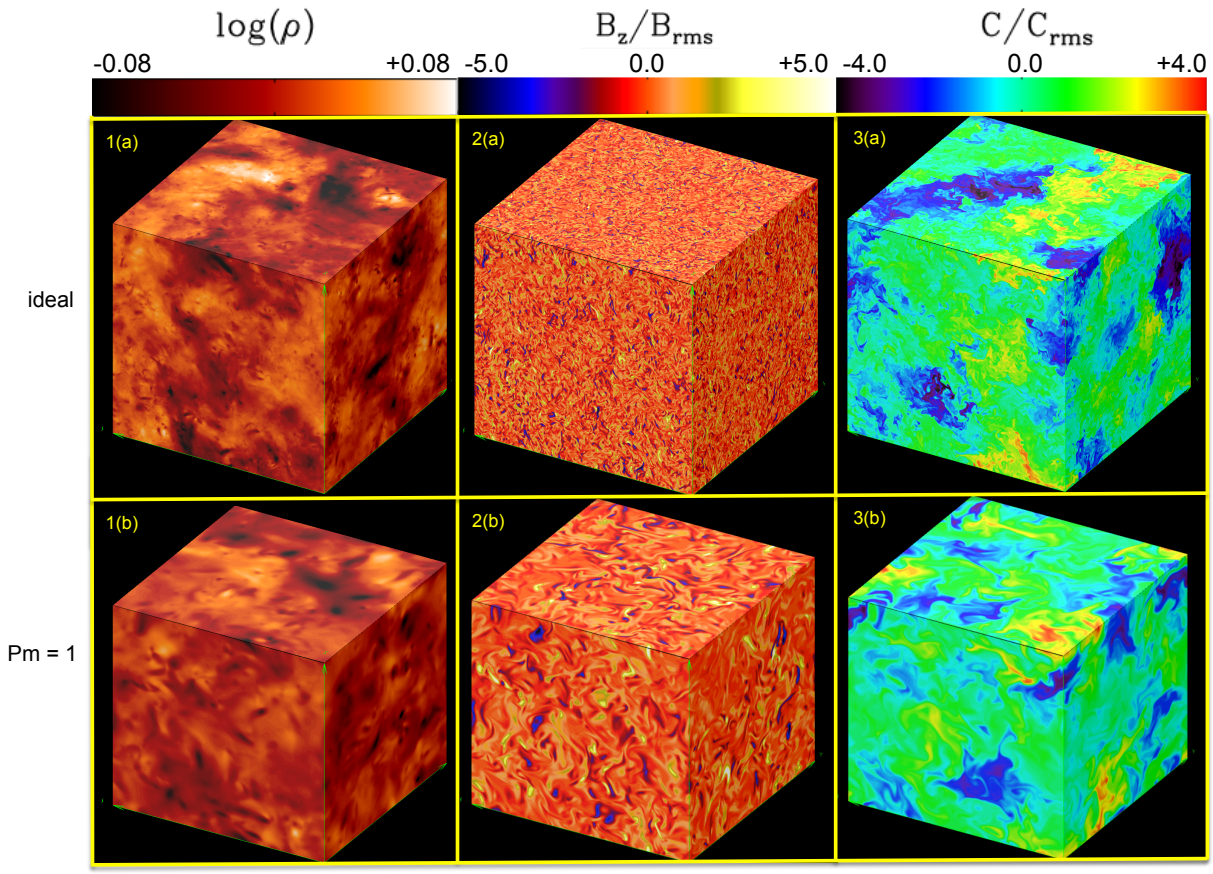

Figure 2. Three dimensional volume rendering from the ideal (first row) and the non-ideal (second row) runs at $\mathcal{M} = 0.3$, $\beta_{\rm in} = 10^7$, M0.3Id2 and M0.3Pm1b. The panels show showing the density (panels 1a and 1b), the z-component of the magnetic field normalized by the rms magnetic field $\rm B_z/B_{rms}$ (panels 2a and 2b) and the scalar concentration field normalized by the rms value (panels 3a and 3b) on the periphery of the simulation volume at $t \simeq 2.5 t_{\rm ed}$. This corresponds to the kinematic phase of the dynamo. Note the initial weak vertical magnetic field is deformed by the underlying turbulence and resembles white noise.

and saturated phases of evolution. In the first column (panels 1a, 1b and 1c), we compare the power spectra obtained from the ideal MHD run to that of the non-ideal run at $\mathcal{M} = 0.3$. Because the viscous scale is larger for the non-ideal run, the turnover point for this run lies at smaller k. Nevertheless, over the inertial range, the velocity power spectra for both the ideal and the non-ideal run have a $\approx k^{-5/3}$ scaling in the kinematic phase (dotted red and blue dashed lines), measured from runs with $\beta_{\rm in} = 10^7$. The power spectrum peaks at $k/2\pi = 2$ which corresponds to the energy injection scale in our simulations. In the saturated phase, the velocity spectrum has a slightly steeper scaling in the range $k \sim (3-9)$ which can be attributed to energy transfer from $E_{\rm k}$ to $E_{\rm m}$ which occurs faster at smaller scales. A simple linear regression analysis gives the best-fit slope to be $\approx k^{-1.85}$.

The magnetic power spectra plotted in panel 1(b) show the evolution in the kinematic and saturated phases of the dynamo. At low k, the magnetic field spectra are flatter than the Kazantsev $k^{3/2}$ scaling at early times (Kazantsev 1968; Brandenburg & Subramanian 2005; Bhat & Subramanian 2013) although still peaked at much larger scales at $k \approx 20$ for the non-ideal run and at about $k \approx 40$ for the ideal run. This difference is again because of the larger inertial range available in the ideal case which leads to a lot more eddies amplifying the field at smaller scales compared to the non-ideal run at Pm = 1. If u_l is the velocity fluctuations on a scale l, then $t_{\rm ed} = l/u_l \propto l^{2/3}$ for Kolmogorov turbulence. Thus, smaller eddies amplify the magnetic field faster because of their shorter turnover times and hence the magnetic power spectrum initially peaks at large k. However, as the magnetic field approaches saturation, the peak of the magnetic spectrum shifts to larger scales at about $k \approx 4$, implying an increase in the coherence length of the field. This feature can also be seen in the three-dimensional volume rendering plots upon comparing panels 2(b) in Figs. 2 and 3.

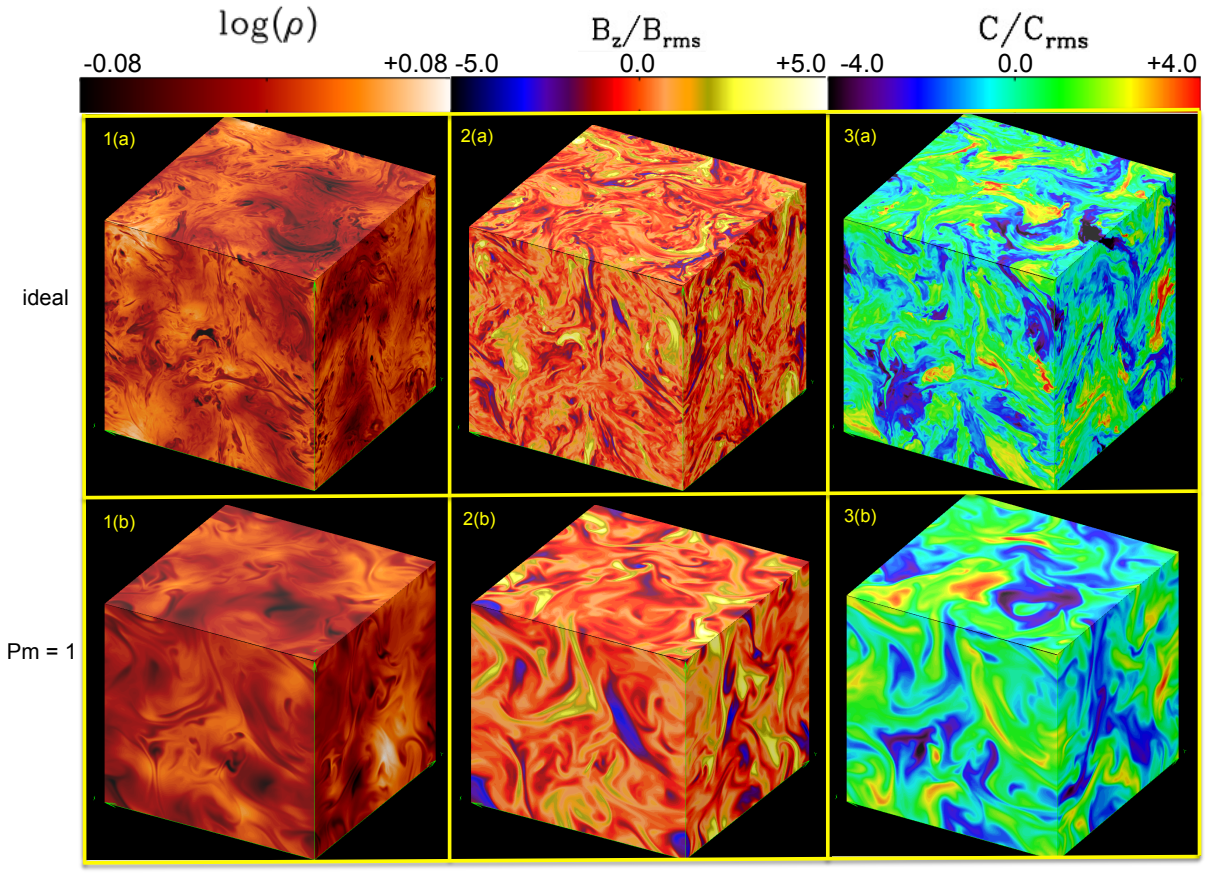

Figure 3. Same as in Fig. 2 but now at $t \simeq 8.8 t_{\rm ed}$ when the magnetic field is saturated, obtained from runs M0.3Id1 and M0.3Pm1a. Note the presence of long filamentary structures in both the magnetic field and the scalar concentration field compared to the ones in Fig. 2.

In Figure 4, panel 1(c) shows the time evolution of the scalar power spectrum. The classical picture for the generation of scalar structures at small scales is a cascade process that is similar to the cascade of the velocity field, resulting in a $k^{-5/3}$ scalar spectrum for isotropic incompressible turbulence (Sreenivasan 1996; Watanabe & Gotoh 2004). Since we use three independent scalars, the power spectrum is averaged over the three values at each k, increasing the accuracy of our measurements. For the modest Reynolds numbers ≈ 1250 achieved in our simulations, we find a $k^{-5/3}$ scaling in a narrow band of wave numbers $k \approx (3-8)$ in the kinematic phase which then becomes flatter $\approx k^{-4/3}$ in the saturated phase. We note here that measuring the scalar spectrum slope accurately is somewhat ambiguous because of the sudden drop in the spectrum from $k = 2$ to 3. The best fit scaling seems to be more like $k^{-1.15}$ for the saturated phase.

Comparing panels 1(a) and 1(c) we find that the slope of the velocity spectra decreases as the system evolves from the kinematic to the saturated state. However, the slope of the scalar power spectrum increases. As the system approaches saturation, the Lorentz forces become strong enough to affect the velocity field thereby reducing the velocity fluctuations. This leads to an increase in scalar fluctuations and hence a flatter scalar power spectrum. If α_u and α_c are the scaling exponents of the velocity and the scalar power spectrum respectively, then the OC theory predicts

$$\alpha_c = -\left[\frac{5+\alpha_u}{2}\right], \tag{8}$$

as described in more detail below. In the kinematic phase, for $\alpha_u = -5/3$, the above relation predicts $\alpha_c = -5/3$ which is in perfect agreement with the slopes obtained in our simulations. In the saturated phase where $\alpha_u = -1.85$ as obtained from our best-fit model, $\alpha_c = -1.57$ which is slightly steeper than the $\approx k^{-1.15}$ scaling we obtain in our simulations. Note however that because the inertial range is small in our simulations and, more importantly, because $E_k(k)$ and $E_c(k)$ in the saturated phase may not be strictly power laws, a perfect match between these models is not expected. Similarly,

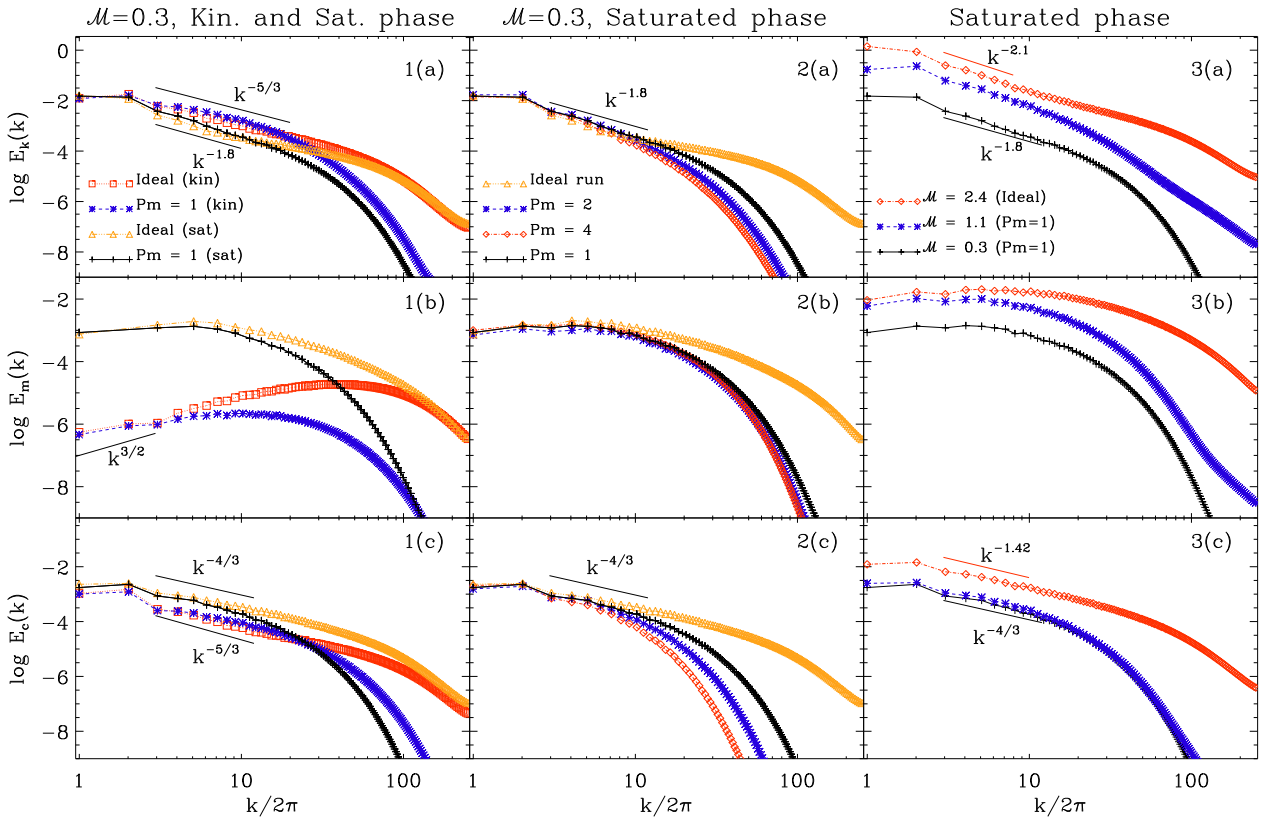

Figure 4. Power spectra of the velocity, magnetic and the scalar field - for the kinematic and saturated phase of evolution at $\mathcal{M} = 0.3$ (column 1), as a function of different Prandtl numbers for $\mathcal{M} = 0.3$ in the saturated state of the dynamo (column 2) and as function of different Mach numbers for a Prandtl number of unity (column 3). The errors in the estimate of the power spectra are less than 10% of their values.

the best-fit k space power-law and the structure function power law fits below are expected to show the same trends, but not necessary exactly obey $\alpha = -(1 + \xi)$, where ξ is the structure function slope, as pure power laws would do.

In the second column, we plot the velocity, magnetic and the scalar power spectra for runs with $\mathcal{M} = 0.3$ in the saturated state for different Prandtl numbers. As stated earlier, for our high Pm runs, we decrease the fluid Reynolds number, keeping the magnetic Reynolds number unchanged. Therefore, as we go from Pm = 1 to 4, the viscous scale moves to smaller k values for both the velocity and the scalar spectra as evident from panels 2(a) and 2(c). However, the slope of the velocity power spectrum appears to be independent of Pm and has the same $\approx k^{-1.8}$ scaling in the range $k \approx 3-8$ for the range of magnetic Prandtl numbers explored in this study. One would expect the velocity spectra to become steeper with increasing Pm as the fluid becomes increasingly viscous. On the other hand, the dissipation scale for the magnetic field remains independent of the change in Pm because Rm is the same for all the runs. In the case of the scalar concentration field, the slope of the spectrum is flatter $\approx k^{-4/3}$ for the ideal and the Pm $= 1, 2$ non-ideal runs in the range $k \approx 3 - 7$ while for Pm = 4, the above scaling holds only for a very short range of $k \sim 3 - 5$.

In the third column, we show the power spectra in the saturated phase for the different Mach numbers. In particular, we plot the velocity, magnetic and the scalar spectra for M0.3Id2, M2.4Id and M0.3Pm1a runs. As evident from panel 3(a), the velocity power spectrum for $\mathcal{M} = 2.4$ shows a $\approx k^{-2.1}$ scaling in the saturated phase. In the kinematic phase, the velocity spectrum shows a $\approx k^{-2}$ scaling resulting from the dominance of shocks in the turbulent flow (e.g. Pan & Scannapieco 2010). Together with the increase in shock intensity with increasing Mach numbers and the fact that the pressure term preferentially converts kinetic to thermal energy thereby resulting in the loss of kinetic energy along the cascade causes the velocity spectrum to be much steeper than the subsonic case. However, the steepening of the spectrum in the saturated phase has to do with the velocity fluctuations being dominated by the magnetic field leading to the familiar behavior seen in our saturated runs (see panel 2a). In this phase, the scalar power spectra shows a $k^{-1.42}$ scaling for $\mathcal{M} = 2.4$ while a $k^{-1.4}$ for the other two runs. The best-fit scaling for $\mathcal{M} = 2.4$ is $\approx k^{-1.44}$ while the scaling predicted from eq. (8) is $\approx k^{-1.45}$.

In addition, we also computed the evolution of the integral scale of the velocity, magnetic and the scalar concentration field for the simulation runs presented here. The velocity and the magnetic integral scale evolution has been previously reported in the works of Cho & Ryu (2009) and Bhat & Subramanian (2013). We find that while the velocity and the scalar integral scale remains almost constant, the integral scale for the magnetic field increases by a factor of $\sim 3-4$ as the system evolves from the kinematic to the saturated phase. This increase is consistent with the results reported in Cho & Ryu (2009) and Bhat & Subramanian (2013) and can explain the gradual increase in coherence scale of the magnetic field structures seen by comparing Figs. 2 and 3.

3.3.2. *Structure Functions and Dimensionality of Scalar Structures*

In this subsection, we analyze the scaling properties of the second order longitudinal velocity structure functions (SFs), defined as $S^u_{||}(l) \equiv \langle[(\boldsymbol{u}(\boldsymbol{x}+\boldsymbol{l})-\boldsymbol{u}(\boldsymbol{x}))\cdot\boldsymbol{l}/l]^2\rangle$ and the scalar structure function $S_C(l) \equiv \langle(C(\boldsymbol{x}+\boldsymbol{l}) - C(\boldsymbol{x}))^2\rangle$, where l is the separation distance. Figure 5 shows a plot of $S^u_{||}(l)$ (upper panel) and $S_C(l)$ (lower panel) in our M0.3Id2 run, for three different phases. In the kinematic phase, when the magnetic field is dynamically unimportant, the velocity structure function shows an $l^{2/3}$ scaling, in perfect agreement with the predictions of the Kolmogorov theory. In the saturated phase, this scaling steepens to $\approx l^{1.05}$. A similar behavior was also observed from the velocity power spectra plots in Fig. 4 which shows the slope of the velocity spectra to be slightly steeper than $k^{-5/3}$ in the saturated regime. Physically this is due to the transfer of the kinetic to magnetic energy, and it occurs faster at smaller scales, leading to a steepening of the velocity structure function or spectra. A supporting evidence is that the structure function, $\langle[(\mathbf{u}(\boldsymbol{x}+\boldsymbol{l})-\mathbf{u}(\boldsymbol{x}))\cdot\boldsymbol{l}/l]^2\rangle + \frac{1}{4\pi}\langle[(\mathbf{B}(\boldsymbol{x}+\boldsymbol{l}) - \mathbf{B}(\boldsymbol{x}))\cdot\boldsymbol{l}/l]^2\rangle$, corresponding to the sum of the kinetic and magnetic energies, is much shallower, $\propto l^{0.60}$, than the velocity structure function itself. The scaling exponent of $S^u_{||}(l)$ in the intermediate phase (red dashed curve) lies somewhere in between the above two values for the kinematic and saturated phases.

The scalar evolution is regulated by the velocity field (see eqn. 7), and, as a response to the changes in the velocity statistics in two phases, the scalar structure function, $S_C(l)$, also shows different scalings, flattening from $l^{2/3}$ in the kinematic phase to $l^{0.5}$ in the saturated phase. We find that these scaling exponents are consistent with the OC picture, where a constant flux of scalar energy occurs along the cascade over the inertial range. In this range, the scalar fluctuations are determined by the advecting velocity only. If we assume that the timescale for a cascade step is of $\approx O(t_{\rm ed})$ at a given scale, then the difference in scalar concentration over a scale 'l' is related to the velocity difference as

$$\delta C(l)^2 \simeq \bar{\epsilon}_c \frac{l}{\delta u(l)}, \tag{9}$$

where $\bar{\epsilon}_c$ is the scalar dissipation rate. Therefore, if the second order velocity and scalar structure functions are defined as, $\langle\delta u(l)^2\rangle \propto l^{\xi_u}$, and $\langle\delta C(l)^2\rangle \propto l^{\xi_c}$, the scaling exponents are related as

$$\xi_c \simeq 1 - \xi_u/2. \tag{10}$$

Substituting $\xi_u = (0.67, 1.05)$ obtained from Fig. 5, the above relation predicts $\xi_c = (0.665, 0.475)$, in good agreement with $\xi_c = (0.67, 0.50)$ inferred from our simulations as shown in the figure. Repeating this analysis for our supersonic ideal MHD run, M2.4Id we find $\xi_u = (0.85, 0.92)$ and $\xi_c = (0.56, 0.52)$ which are again in good agreement with the scaling exponents obtained from eq. 10. However, since the inertial range obtained from our structure functions are quite narrow even for our ideal MHD runs, we refrain from computing the same for our non-ideal MHD runs which has an even narrower inertial range due to the modest Reynolds numbers achievable in our simulations.

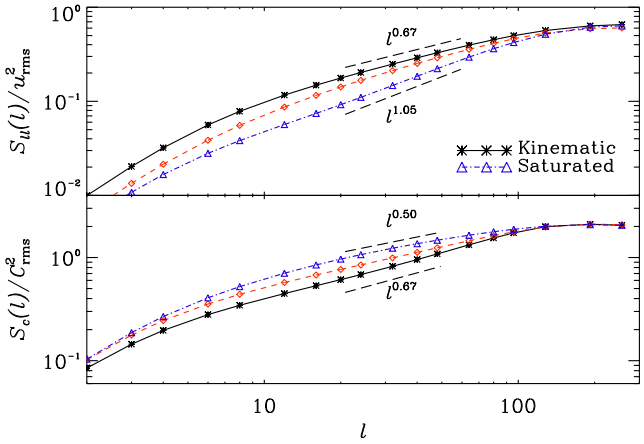

Figure 5. Second order longitudinal velocity structure function (upper panel) and the scalar structure function (lower panel) for run M0.3Id2 in the kinematic (black solid), intermediate (red dashed) and saturated (blue dash dotted) phases. The velocity field scales as $l^{2/3}$ in the kinematic phase and as $l^{1.05}$ in the saturated phase. The scalar concentration field also shows an $l^{2/3}$ scaling in the kinematic but an $l^{1/2}$ in the saturated phase consistent with the OC picture.

We now turn our attention to the nature of the hierarchical structures of the velocity and scalar fields by analyzing structure functions at high orders. At the outset, we define the velocity, scalar and the mixed SF's of order p as,

$$S^u_p(l) \equiv \langle|\delta u(l)|^p\rangle \propto l^{\xi_u(p)}, S^C_p(l) \equiv \langle|\delta C(l)|^p\rangle \propto l^{\xi_C(p)},$$
$$S^m_p(l) \equiv \langle|\delta u(l)\,\delta C(l)^2|^{p/3}\rangle \propto l^{\xi_m(p)}, \tag{11}$$

where $\delta u(l)$ and δC are the longitudinal velocity and

scalar increments at a distance of l. The She-Leveque (SL) (She & Leveque 1994) intermittency model gives a prediction for the scaling exponent $\xi(p)$,

$$\xi(p) = \gamma p + C(1 - \beta_i^p), \tag{12}$$

where β_i is the intermittency parameter, γ is the scaling exponent for the most intense structures, and C is interpreted as the codimension of these structures, such that fraction dimension is $d = 3 - C$ for three-dimensional flows. The model can thus be used to study the geometry of the strong velocity or scalar structures. Because of the limited inertial range available in our turbulence simulations, it is difficult to measure $\xi(p)$ at high orders. In such cases, it turns out that one can exploit the self-similarity hypothesis of Benzi et al. (1993) to measure the SF's at all orders against the third order ones, which allows for an extended power-law range and more accurate measurements. We therefore measure the scaling exponents $\zeta(p)$ relative to the third order SF's defined as $S_p(l) \propto [S_3(l)]^{\zeta(p)}$. By definition, $\zeta(p) = \xi(p)/\xi(3)$ and $\zeta(3) = 1$.

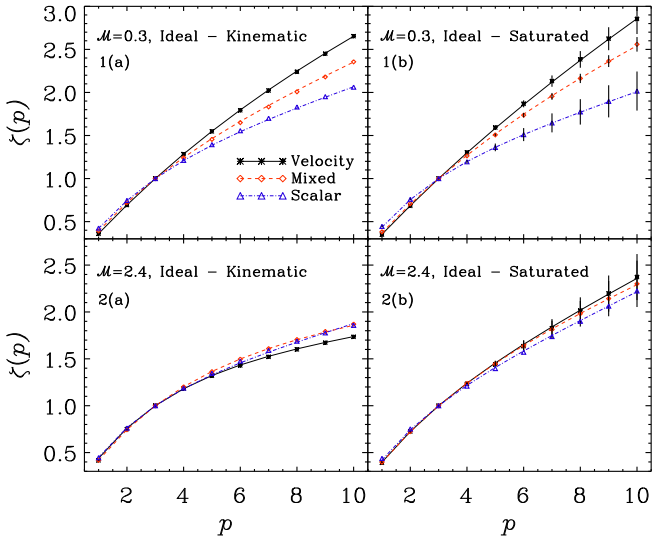

Figure 6. Scaling exponents ζ_p for the SF's in the kinematic and saturated phases for runs : M0.3Id2 (upper row) and M2.4Id (bottom row). Black vertical lines in the panels depict the error bars. The scalar field appears to be more intermittent than the velocity in both the phases for $\mathcal{M} = 0.3$ while the velocity appears to be more intermittent at $\mathcal{M} = 2.4$.

In Fig. 6, we plot the scaling exponents ζ_p for the velocity, scalar and the mixed SF's for the ideal runs with $\mathcal{M} = 0.3$ (upper row) and 2.4 (bottom row). We find that for all p, the values of ζ_p are consistent with the generalized SL model,

$$\zeta(p) = \gamma' p + C' (1 - \beta_i^p), \tag{13}$$

where $\gamma' = \gamma/\xi(3)$ and $C' = C/\xi(3)$ and $\xi(3)$ denotes the scaling exponent of the third order SF. The vertical lines show the error bars, corresponding to the snapshot-to-snapshot variations. For the subsonic run, the scaling exponents in the left panel for the kinematic phase were measured from a single snapshot in the kinematic phase, as the number of snapshots available in the run after the flow is fully developed but before the magnetic field becomes dynamically important is very limited.

We first discuss the results for the subsonic flow. In the top left panel of Fig. 6, we see that ζ_C is smaller than both ζ_u and ζ_m in the kinematic phase, implying that the scalar structures are more intermittent than the velocity field. This is consistent with results of earlier studies for turbulent mixing in incompressible or weakly compressible hydrodynamical flows (e.g., Pan & Scannapieco 2011). The exponents of the mixed structures lie in between the velocity and scalar structures as expected. In the saturated phase (panel 1b), ζ_C, ζ_m, and ζ_u are in the same relative order, and a comparison of the two panels shows that the velocity field in the saturated phase is less intermittent than in the kinetic phase, suggesting that the presence of the magnetic tension and pressure tends to suppress the development of intense velocity structures.

Note that ζ_u measured here is not to be confused with the scaling exponents for the Elsässer variables $z_\pm \equiv u \pm B/\sqrt{4\pi}$ commonly analyzed in incompressible MHD turbulence studies. We also attempted to measure the scaling of $z_\pm$ in our flow, and found that their scaling exponents are more intermittent than those (ζ_u) for the velocity field itself (see Haugen et al. 2004). A likely reason is that the existence of the strong magnetic structure such as the current sheets contributes to the intermittency of $z_\pm$. We point out that the difference in the scaling properties of the velocity field from $z_\pm$ suggests that the most intermittent velocity structures may have different locations from the strong magnetic structures, such as the current sheets. Here, for the study of mixing, we are mainly concerned with the velocity structures, and thus choose not to show the scalings of $z_\pm$.

In our subsonic flow with Mach 0.3, the scaling exponents, ζ_C, normalized to the 3rd order structure function for the scalar field in the kinematic and saturated phases are very close to each other. However, the unnormalized exponents, ξ_C, for the scalar field in the two phases are different due to the difference in $\xi(3)$. This may be responsible for the different visual impressions in the scalar images shown in Figs. 2 and 3.

As the flow Mach number changes from 0.3 to 2.4, the velocity field in the kinematic phase becomes significantly more intermittent, consistent with the earlier results of Pan & Scannapieco (2011) for mixing in hydrodynamical flows. This is due to the formation of shocks, which are intense dissipative structures and are known to increase the intermittency of the velocity field. On the other hand, the intermittency of the scalar structures only changes slightly as the flow goes from subsonic to supersonic. The reason is that the existence of velocity shocks do not cause discontinuities in the scalar field.

Since the flow and pollutant densities are both conserved across velocity shocks, the concentration field and the ratio of two densities, remains continuous (Pan & Scannapieco (2011)). This explains the small changes in the scaling exponent, ζ_C, of the scalar field, despite the significantly higher intermittency in the velocity field. In comparison to the subsonic case, the relative degree of intermittency is reversed with the velocity structures being slightly more intermittent the scalar field.

As the magnetic field grows, the formation of shocks is expected to be suppressed, as the magnetic field along the shock front has the effect of opposing the converging flow, like the effect of the thermal pressure. Therefore, once the Alfvénic speed becomes comparable to or larger than the sound speed, the frequency and the strength of the shocks would be reduced. As a result, the velocity structures in the saturated phase become significantly less intermittent than in the kinematic phase. The scaling of the concentration field is less affected by the growth of the magnetic strength, again because it is insensitive on whether velocity shocks exist. Roughly speaking, as the magnetic strength saturates in our $\mathcal{M} = 2.4$ flow, the Alfvénic Mach number, which is smaller then sonic Mach number, would play the role of the sonic Mach number. The result that the velocity scaling is less intermittent than the scalar field in the saturated phase could be viewed as corresponding to a case with an effective Mach number significantly smaller than 2.4 (see Pan & Scannapieco (2011)).

In summary, the scaling of the velocity structures has a significant dependence on both the flow Mach number and the magnetic strength. The velocity intermittency increases with increasing Mach number, and decreases as the magnetic field becomes dynamically important and suppresses shock formation. On the other hand, the scaling behaviors of the scalar field are insensitive to velocity shocks, which do not produce concentration discontinuities, and thus show only slight changes with the Mach number and/or the magnetic growth.

Following Pan & Scannapieco (2011), we measured the parameter β_i using the structure function ratios, $F_p(r) = S_{p+1}(r)/S_p(r)$, at successive orders. The slope of the $F_{p+1}(r)/F_2(r)$ vs. $F_p(r)/F_1(r)$ curves at given orders, p, provides an estimate for β_i (She et al. 2001). The values of C' are then obtained by fitting the data points for ζ_p as a function of p shown in the above figure. Using the measured C' and the values of $\xi(3)$ from the third order SF's, we estimate the fractal dimension $d = 3 - \xi(3)C'$ of the velocity, mixed and the scalar fields. Table 2 summarizes the scaling exponents of the third order structure functions, the parameter β_i and the fractal dimension d for the velocity, mixed and the scalar field corresponding to two ideal runs, M0.3Id2 and M2.4Id. The parameters given in the table for the kinematic phase are consistent with those obtained in earlier studies for incompressible or weakly compressible flow. The scaling exponent, $\xi_m(3)$, for the third-order mixed structure function is close to unity in both phases, confirming the general validity the scalar cascade picture.

We find that for each type of structures, the velocity, mixed or scalar, there exists a narrow range of β_i around the values listed in Table 2 that can fit $\zeta(p)$ will as a function of p. In such a range of β_i, one can tune the parameter C' to obtain satisfactory fits to $\zeta(p)$. It turns out that, for the velocity structures in the subsonic run, especially in the saturated phase, the best-fit C' and hence d have a very sensitive dependence on the choice of β_i. For example, if we set β_i^u in the saturated phase to 0.86, the best-fit C'_u would be 1.05 and thus $d_u = 1.53$. On the other hand, if we increase β_i^u slightly to 0.90, we obtained $C'_u = 2$ and $d_u = 0.2$. Such a sensitive dependence suggests that d_u cannot be measured reliably unless β_i^u can be determined at an accuracy level $\ll 1\%$. Such an accuracy level is not possible in our simulations, the definite determination of the dimension of the strong velocity structures in the saturated phase requires high-resolution simulations that allow a broad inertial range. For the mixed and scalar structures and all the three kinds of structures in the supersonic run, the dependence of C' or d on the selected value of β_i is much weaker than in the velocity case, and the measured values of d are thus reliable at least qualitatively.

For M0.3Id2 run, the fractal dimension d_C for the scalars changes slightly from 2.15 in the kinematic phase to 2.41 in the saturated phase, suggesting that the strong scalar structures continue to be sheet-like as the magnetic field grows to saturation. A very similar change in the scalar dimension is observed in the supersonic case. The slightly larger d_C in the saturated phase appears to be consistent with the morphological differences in Figs. 2 and 3, and is likely arises because the Lorentz force resists compression, and thus cliffs become thicker. The dimensionality of the strong scalar structures may be understood by an analysis of the strain tensor. For example, if the scalar field is compressed in two directions, then the scalar structures would tend to be filamentary. On the other hand, our finding of sheet-like scalar structures in both phases implies that the strain tensor compresses the scalar field in one direction and extends it in the other two directions. We will perform a more detailed study of the strain tensor and its relation to the magnetic and concentration field structures in a future work.

3.4. *Scalar Dissipation and Mixing Timescale*

The small-scale dynamo generates magnetic fields that are random in both space and time as evident from Figs. 2 and 3. At the same time, turbulent eddies also stretch the scalar concentration field forming similar random small-scale structures. Here, we explore how the turbulent mixing varies as a function of the magnetic field and how does the mixing time scale depends on the Prandtl and Peclet numbers and the Mach number of the flow. To study this effect, we compute the mean of the scalar dissipation $\langle\tilde{\rho}(\nabla C)^2\rangle$ conditioned on the magnetic field strength, where again $\tilde{\rho} \equiv \rho/\overline{\rho}$ is the ratio of the density ρ to the average flow density, $\overline{\rho}$. As is clear from

$\mathcal{M}$	$\xi_u(3)$		β_i^u		d_u		$\xi_m(3)$		β_i^m		d_m		$\xi_C(3)$		β_i^C		d_C	
	Kin.,	Sat.	Kin.,	Sat.	Kin.,	Sat.	Kin.,	Sat.	Kin.,	Sat.	Kin.,	Sat.	Kin.,	Sat.	Kin.,	Sat.	Kin.,	Sat.
0.3	0.98	1.40	0.88	0.88	1.04	1.00	0.96	0.96	0.74	0.81	2.08	1.84	0.87	0.65	0.68	0.64	2.15	2.41
2.4	1.15	1.33	0.70	0.70	1.50	1.94	0.95	0.96	0.75	0.74	1.58	2.03	0.78	0.71	0.63	0.63	2.25	2.47

Table 2
Scaling exponent $\xi(3)$ of the third order SF's, intermittency parameter β_i and the fractal dimension d of the most intense structures for M0.3Id2 and M2.4Id runs.

eq. (7), scalar dissipation is strongest in regions in which $\tilde{\rho}(\nabla C)^2$ is large, which reduces to $(\nabla C)^2$ in the incompressible limit. As large scalar gradients would therefore imply efficient mixing, it is important to study how $\tilde{\rho}(\nabla C)^2$ varies in regions with different magnetic field strengths, as produced by a small-scale dynamo.

We show the results obtained from the various runs in Table 3. For subsonic turbulence, $\langle\tilde{\rho}(\nabla C)^2\rangle$ increases with increasing field strength in the kinematic phase. Because this occurs in a phase in which the magnetic field is unimportant, this implies that magnetic field amplification and scalar gradients are both increased by the same overall properties of the local flow, in particular, the velocity gradient. In fact, a simultaneous increase of both these quantities is expected in regions in which the flow is contracting relative to the direction of the local magnetic field, as this would both increase the field amplitude by flux freezing, and simultaneously increase the scalar gradient in the direction of the contraction. In the saturated phase, on the other hand, $\langle\tilde{\rho}(\nabla C)^2\rangle$ increases with increasing field strength at low magnetic field values, and then decreases with increasing magnetic field strength, hinting at Lorentz forces inhibiting the buildup of large scalar gradients.

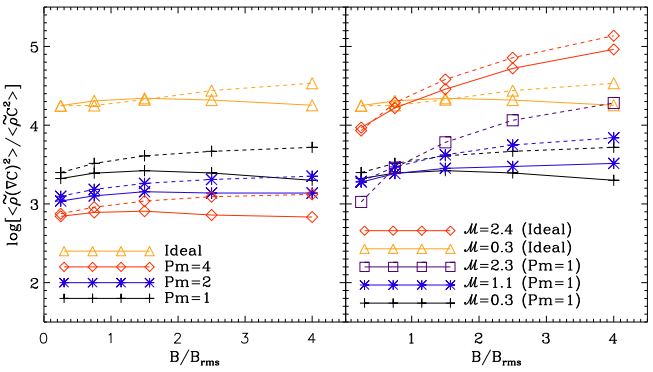

Figure 7. The values of $\langle\tilde{\rho}(\nabla C)^2\rangle/\langle\tilde{\rho}C^2\rangle$ for the different Pm runs in the left panel and for the different Mach number runs in the right panel. Dashed lines denote the kinematic phase while the solid lines are for the saturated phase.

We observe these trends to hold irrespective of the magnetic Prandtl numbers, although the overall magnitude of $\langle\tilde{\rho}(\nabla C)^2\rangle$ decreases strongly with Pm, as expected because increasing κ will increase the length scale of typical scalar structures. On the other hand, for $\mathcal{M} = 1.1$ and 2.4 the scalar dissipation, $\langle\tilde{\rho}(\nabla C)^2\rangle$ continues to increase monotonically with the magnetic field strength in both the kinematic and saturated phases. This is most likely due to the fact that the ratio of the magnetic to kinetic energies, $E_{\rm m}/E_{\rm k}$ is still low even in the saturated phase compared to the subsonic runs. The monotonic increase of $\langle\tilde{\rho}(\nabla C)^2\rangle$ is the strongest for M2.4Id run among all the runs reported here. Since we could only follow the M2.3Pm1 run till the linear growth phase, we only show the corresponding values for the kinematic phase. For reference, in the last column in Table 3, we give the overall density-weighted concentration variance $\langle\tilde{\rho}C^2\rangle$, not conditioned on the magnetic field strength. In Figure 7, we show the conditional dissipation rate normalized to the variance $\langle\tilde{\rho}C^2\rangle$, as a function of the magnetic strength. Clearly, the normalization provides a better measure for the mixing efficiency. In general, the normalized conditional dissipation in the saturated phase is lower than in the kinematic phase, again supporting the argument that strong magnetic fields tend to slow down the buildup of the scalar gradients.

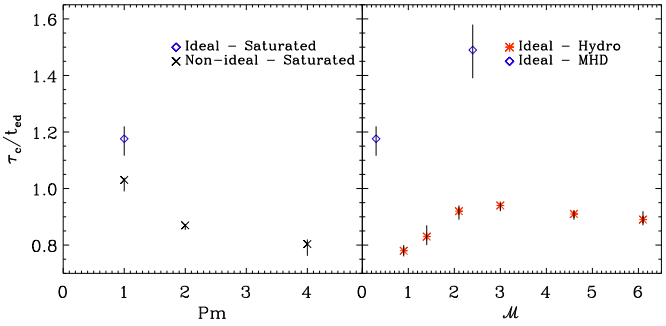

Figure 8. Dependence of the mixing time scale τ_c on flow properties. In the left panel, labeled as a function of Prandtl number, we see that the mixing timescale in the saturated phase decreases as the magnetic resistivity is held fixed, and viscosity and scalar diffusivity are increased simultaneously. In the right panel, the mixing time scale in ideal runs with varying Mach number are plotted in the saturated phase (diamonds) and from purely hydrodynamical simulations (asterisks, Pan & Scannapieco 2010) In both panels the solid vertical lines denote error bars.

Finally, we computed the overall rate of mixing as a function of Prandtl number and Mach number. In the presence of a physical scalar diffusivity, the mixing time

Simulation Run	$\langle\tilde{\rho}(\nabla C)^2\rangle$	$\langle\tilde{\rho}(\nabla C)^2\rangle$ $\frac{B}{B_{\rm rms}} \le 0.5$	$\langle\tilde{\rho}(\nabla C)^2\rangle$ $0.5 < \frac{B}{B_{\rm rms}} \le 1.0$	$\langle\tilde{\rho}(\nabla C)^2\rangle$ $1 < \frac{B}{B_{\rm rms}} \le 2$	$\langle\tilde{\rho}(\nabla C)^2\rangle$ $2\frac{B}{B_{\rm rms}} \le 3$	$\langle\tilde{\rho}(\nabla C)^2\rangle$ $3 < \frac{B}{B_{\rm rms}} \le 5$	$100 \times \langle\tilde{\rho}C^2\rangle$
	Kin., Sat.	Kin., Sat.	Kin., Sat.	Kin., Sat.	Kin., Sat.,	Kin., Sat.	Kin., Sat.
M0.3Id2	107, 197	107, 175	108, 201	128, 217	167, 206	207, 177	0.607, 0.988
M0.3Pm1a	19.6, 20.6	15.2, 18.1	19.9, 21.2	24.8, 22.8	28.3, 21.3	31.8, 17.2	0.608, 0.862
M0.3Pm2	8.85, 9.35	7.34, 8.07	8.98, 9.40	10.7, 10.6	12.0, 10.2	13.2, 10.2	0.587, 0.742
M0.3Pm4	4.87, 5.07	4.07, 4.70	4.94, 5.26	5.90, 5.46	6.70, 4.88	7.18, 4.60	0.543, 0.675
M1.1Pm1	21.6, 24.1	14.2, 18.9	21.7, 24.3	30.9, 28.3	41.2, 29.9	50.8, 32.7	0.735, 1.00
M2.4Id	178, 281	74.0, 137	167, 243	330, 421	622, 774	1184, 1350	0.866, 1.47
M2.3Pm1	27.2, –	9.64, –	26.2, –	55.14, –	105, –	174, –	0.910, –

Table 3

Mean values of $\langle\tilde{\rho}(\nabla C)^2\rangle$ for the different simulation runs in both the kinematic and saturated phases. The overall values of the scalar dissipation are tabulated in the second column while the values conditioned on the magnetic field strength are presented in the 3rd to the 7th columns. For reference, $\langle\tilde{\rho}C^2\rangle$ is presented in the 8th column

. For M2.3Pm1, we only show the values in the kinematic phase. Note that while all the values in this table can be rescaled by a single arbitrary number, corresponding to the strength of the scalar driving, the relative values can be accurately compared across runs, across magnetic field ranges, and between the kinematic and saturated phases.

scale $\tau_{\rm c}$ is defined as

$$\tau_c = \langle\tilde{\rho}C^2\rangle/\overline{\epsilon}_c = \langle\tilde{\rho}C^2\rangle/2\langle\tilde{\rho}\kappa(\nabla C)^2\rangle, \qquad (14)$$

where $\overline{\epsilon}_c = 2\langle\tilde{\rho}\kappa(\nabla C)^2\rangle$ is the scalar dissipation rate. In ideal MHD, the above definition no longer holds since the scalar diffusivity is of numerical origin. However, as can be seen from eq. (7), in the statistically homogeneous case, one can still define a mixing time scale by assuming a balance between the scalar dissipation rate and the scalar source term when scalar fluctuations reach a statistically stationary state (Pan & Scannapieco 2010). This then leads to a dissipation time scale, $\tau_c = \langle\tilde{\rho}C^2\rangle/\overline{\epsilon}_s = \langle\tilde{\rho}C^2\rangle/\langle\tilde{\rho}TC\rangle$ where $\overline{\epsilon}_s = \langle\tilde{\rho}TC\rangle$ denotes the source term for scalar fluctuations. To check the validity of this assumption we computed τ_c by both the methods for one of our non-ideal runs (M0.3Pm1a) and find the two time scales to be similar got $t \ge 5\,t_{\rm ed}$.

In Figure 8, we show the dependence of the mixing time scale $\tau_{\rm c}$ normalized to the eddy turnover time on the magnetic Prandtl number Pm (left panel) and Mach number (right panel) when the magnetic field has reached saturation. The mixing time scale shows a weak dependence on the magnetic Prandtl number with the timescale decreasing with increasing Prandtl number. As discussed above, we increase the viscosity and scalar diffusivity simultaneously, in our simulations to obtain Pm > 1. This results in a drop of Reynolds and Peclet numbers from Re = Pe from 1250 for Pm $= 1$ to ≈ 312 for Pm $= 4$. In other words, the fluid tends to become more viscous, and, likely more importantly, κ becomes higher, making scalar diffusion more effective and reducing the mixing time scale. Note that we have assumed that Pm $\approx O(1)$ for the ideal run.

In the presence of magnetic fields, the mixing time scale increases with increasing Mach number as can be seen from the right panel in Fig. 8. As first measured in Pan & Scannapieco (2010) and also shown in this figure, this trend holds even for pure hydrodynamical runs where the time scale increases with the increase in Mach number from $\mathcal{M} = 0.9$ to 3.0 and thereafter remains constant. Moreover, for a given Mach number, the time scale in the MHD case is higher than its hydrodynamic counterpart, which suggests that the presence of magnetic fields slows down the mixing process. This is consistent with a physical picture in which the magnetic tension resists the straining of the flow, thereby leading to a decrease in the rate of stretching.

4. SUMMARY AND CONCLUSIONS

Magnetic fields are ubiquitous in a wide variety of astrophysical objects ranging from molecular clouds to galaxies and galaxy clusters, as they are both amplified and maintained by turbulence. Such random motions are driven by many sources ranging from supernovae in the ISM (de Avillez & Breitschwerdt 2005; Hill et al. 2012; Gent et al. 2013) to structure formation and active galactic nuclei in galaxy clusters (Norman & Bryan 1999; Ryu et al. 2008, 2012). They are also responsible for the turbulent mixing of elements, which is essential for metal enrichment in the IGM, the pollution of the primordial gas by the first generation of stars, and our interpretation of a variety of observations such as the metallicity dispersion in open clusters, the abundance scatter in the ISM, and the cluster to cluster metallicity scatter. Here we have carried out a systematic investigation into the impact of magnetic fields on turbulent mixing by performing three-dimensional simulations of forced turbulence in a box including magnetic fields and the injection of pollutants at regular intervals. With this setup, we have explored two different parameter regimes consisting of simulations with different magnetic Prandtl numbers, Pm $= 1, 2$ and 4 for $\mathcal{M} = 0.3$, and runs with varying Mach numbers, $\mathcal{M} = 0.3, 1.1$ and 2.3 for Pm $= 1$. In addition, we have also performed ideal simulations to compare with our non-ideal runs at $\mathcal{M} = 0.3$ and at 2.4.

Small-scale dynamo action initially amplifies the magnetic fields exponentially, then linearly, and eventually saturates when energy equipartition is reached on scales

close to the driving scale of turbulence. The saturated phase of the small-scale dynamo is crucial to our studies since, in this phase, the field is strong enough to back-react on the flow and affect its mixing properties. Due to physical viscosities and diffusivities in our non-ideal simulations, the magnetic and the scalar field structures appear to be thicker than their ideal MHD counterparts (see Figs. 2 and 3). Nevertheless, in both cases we find that the magnetic field is strong only in certain regions of the simulation, and that the coherence length of the field increases in the saturated phase. The scalar concentration field also shows sharp contrasts in the kinematic phase, resulting from random stretching and shearing by turbulent eddies. Since most of our simulations begin with $\beta_{\rm in} = 10^4$, we do not have a prominent kinematic growth phase to compute the dependence of the growth rates on the magnetic Prandtl number and the Mach number of the flow. However, we find a decrease in the growth rate of the magnetic field with increasing Mach numbers when comparing the M0.3Id2 and the M2.4Id runs (see inset figure in Fig 1).

In the kinematic phase, the velocity power spectrum for $\mathcal{M} = 0.3$ has a $k^{-5/3}$ slope and the magnetic power spectrum has a slightly flatter scaling compared to the $k^{3/2}$ Kasantsev's scaling. As evident from panel 1(b) in Fig. 4, most of the field amplification in this phase is driven by turbulent eddies on scales close to the dissipation scale, due to their shorter eddy turnover times, and this results in the magnetic energy peaking on small scales. However, like the velocity spectra, the scalar power spectrum shows a $k^{-5/3}$ scaling in the kinematic phase for the subsonic run.

In the saturated phase, the velocity spectrum becomes steeper than $k^{-5/3}$ due to the faster transfer of kinetic energy to magnetic energy at small scales. As a response to the steepening of the velocity spectrum, the scalar spectrum becomes flatter, $k^{-4/3}$, because a decrease in the velocity power at smaller scales implies an increase in the scalar fluctuations. For supersonic, hydrodynamic turbulence, it is well known that the velocity spectrum steepens from $k^{-5/3}$ to k^{-2} due to the dominance of shocks. In the saturated phase, we find that the velocity spectrum for $\mathcal{M} = 2.4$ becomes marginally steeper than k^{-2} scaling due to magnetic back reactions. In this case, the scalar spectra shows a $\approx k^{-1.42}$ scaling compared to the $\approx k^{-4/3}$ scaling for the subsonic and transonic runs in the saturated phase.

We also studied the structure functions (SF's) for the velocity and the concentration fields for our ideal MHD runs at $\mathcal{M} = 0.3, 2.4$ due to their longer inertial range compared to the other non-ideal runs. For the subsonic case, the longitudinal velocity and the scalar SF's at the second order show an $\approx l^{2/3}$ scaling in the kinematic phase as expected. As the magnetic field grows to saturation, the scaling steepens to $l^{1.05}$ for the velocity, while for the concentration it flattens to $l^{1/2}$. In the supersonic case, the second order SF's for the velocity and scalar fields scale as $\approx l^{0.85}$ and $\approx l^{0.56}$ in the kinematic phase, and change to $\approx l^{0.92}$ and $\approx l^{0.52}$, respectively, in the saturated phase. In both cases, the scaling exponents for the concentration and velocity fields agree remarkably well with a relation predicted by the OC picture.

Quantitative analysis of higher order SF's show that, for subsonic turbulence, the scalar concentration field is more intermittent than the velocity field in both the kinematic and the saturated phases. As the magnetic filed increases, the velocity becomes slightly less intermittent, while the scalar intermittency remains roughly unchanged. At a flow Mach number of 2.4, the existence of shocks greatly increases the intermittency of the velocity field in the kinematic phase, making it more intermittent than the scalar field. Interestingly, with the growth of the magnetic field strength to saturation, the formation of shocks is suppressed by the magnetic pressure, and this significantly reduces the intermittency of the velocity field, bringing it back to a level below the scalar intermittency. Our results show that, unlike the velocity structures whose intermittency depends on the existence and strength of shocks, the scalings of high-order scalar structures appear to be insensitive to the flow Mach number or the magnetic growth. Independent of the Mach number of the flow, the strong scalar structures are sheet-like with a fractal dimension $d_c \approx 2$ in both phases of magnetic field evolution. This implies that the effect of an evolving magnetic field on the topology of the strong scalar structures is slight.

We find that the scalar dissipation becomes less efficient as the magnetic field grows from the kinematic phase to saturation. As shown in Fig. 7, when normalized to the scalar variance, the dissipation rate is generally smaller in the saturated phase for both the subsonic and supersonic runs. We analyzed the dissipation rate conditioned on the magnetic field strength and showed that in the saturated phase of the subsonic run the dissipation becomes slower at sufficiently large B, indicating that mixing is hindered in regions with strong magnetic field. These all suggest that the Lorentz force resists the straining of the flow and hence suppressing the buildup of large scalar gradients, leading to slower mixing when the magnetic field reaches saturation. We observe this trend to hold independent of the magnetic Prandtl number. Unlike the subsonic run, in the saturated phase of the supersonic case, the scalar dissipation conditioned on B keeps increasing monotonically with increasing with the magnetic field strength, which can be attributed to the fact that the $E_{\rm m}/E_{\rm k}$ ratio is still low even in the saturated phase.

Analysis of the mixing time scale, τ_c, reveals a weak dependence on the magnetic Prandtl number, with τ_c decreasing with increasing Pm. In our simulations, we have achieved Pm > 1 by decreasing the fluid Reynolds and Peclet numbers simultaneously, making scalar diffusion more effective and reducing the mixing time scale. Most astrophysical systems like galaxies and galaxy clusters have Pm $\gg 1$ and it would be interesting to see how

τ_c changes in this regime. Computationally, attaining such large Pm with a high Re is strongly limited by the resolution of the simulations, but the case with low Re, although not corresponding directly to any astrophysical system, may nevertheless be worthy of a systematic investigation. The mixing time scale increases with increasing Mach number in our simulations. However, more simulations at $\mathcal{M} > 2.4$ are needed to draw definitive conclusions. Earlier simulations of (Pan & Scannapieco 2010) also find an increase in mixing time scale with increasing Mach numbers up to $\mathcal{M} = 3$, beyond which it remains constant.

Our results also show a higher value of τ_c in the MHD case compared to the hydro case at a given Mach number. This is due to the fact that once the magnetic field reaches saturation, magnetic tension will resist the straining of the flow, thereby decreasing the rate of stretching and inhibiting large scalar gradients.

In this paper, we have concentrated on simulations where the Schmidt number Sc = 1. It would be interesting to explore the parameter regime where Sc is different from unity. For example, Sc > 1 would imply that the scalar dissipation scale lies outside the viscous dissipation scale while for Sc < 1, the scalar dissipation scale would lie inside the viscous dissipation scale.

Although pollutants such as metals constitute only a negligible fraction of the cosmic matter budget, they play a crucial role in constraining star formation, tracing feedback from massive stars and supernovae. They also play a dominant role in the cooling of gas thereby affecting large-scale structure formation on a wide range of scales. Our present work provides a first step toward understanding how such processes are influenced by magnetic fields.

SS & ES were supported by the National Science Foundation under grant AST11-03608 and NASA theory grant NNX09AD106. LP acknowledges support from the Clay postdoctoral fellowship at Harvard-Smithsonian Center for Astrophysics. The authors would also like to acknowledge the Advanced Computing Center at Arizona State University (URL: http://a2c2.asu.edu/), the Texas Advanced Computing Center (TACC) at The University of Texas at Austin (URL: http://www.tacc.utexas.edu), and the Extreme Science and Engineering Discovery Environment (XSEDE) for providing HPC resources via grant TG-AST130021 that have contributed to the research results reported within this paper. We would like to thank Robert Fisher, Dongwook Lee and Dean Townsley for helpful discussions. The FLASH code is developed in part by the DOE-supported Alliances Center for Astrophysical Thermonuclear Flashes (ASC) at the University of Chicago.

REFERENCES

Becker, G. D., Rauch, M., & Sargent, W. L. W. 2009, ApJ, 698, 1010
Benzi, R., Biferale, L., Fisher, R. T., et al. 2008, Physical Review Letters, 100, 234503
Benzi, R., Ciliberto, S., Tripiccione, R., et al. 1993, Phys. Rev. E, 48, 29
Beresnyak, A. 2012, Physical Review Letters, 108, 035002
Bhat, P., & Subramanian, K. 2013, MNRAS, 429, 2469
Biermann, L. 1950, Zeitschrift Naturforschung Teil A, 5, 65
Brandenburg, A., Sokoloff, D., & Subramanian, K. 2012, Space Sci. Rev., 169, 123
Brandenburg, A., & Subramanian, K. 2005, Phys. Rep., 417, 1
Bromm, V. 2013, Reports on Progress in Physics, 76, 112901
Brüggen, M., & Scannapieco, E. 2009, MNRAS, 398, 548
Cartledge, S. I. B., Lauroesch, J. T., Meyer, D. M., & Sofia, U. J. 2006, ApJ, 641, 327
Cho, J., & Ryu, D. 2009, ApJ, 705, L90
Cho, J., Vishniac, E. T., Beresnyak, A., Lazarian, A., & Ryu, D. 2009, ApJ, 693, 1449
Churazov, E., Vikhlinin, A., Zhuravleva, I., et al. 2012, MNRAS, 421, 1123
David, L. P., & Nulsen, P. E. J. 2008, ApJ, 689, 837
de Avillez, M. A., & Breitschwerdt, D. 2005, A&A, 436, 585
de Avillez, M. A., & Mac Low, M.-M. 2002, ApJ, 581, 1047
De Silva, G. M., Sneden, C., Paulson, D. B., et al. 2006, AJ, 131, 455
Dimotakis, P. E. 2005, Annual Review of Fluid Mechanics, 37, 329
Eswaran, V., & Pope, S. B. 1988, Physics of Fluids, 31, 506
Federrath, C., Chabrier, G., Schober, J., et al. 2011a, Physical Review Letters, 107, 114504
Federrath, C., Sur, S., Schleicher, D. R. G., Banerjee, R., & Klessen, R. S. 2011b, ApJ, 731, 62
Friel, E. D., & Boesgaard, A. M. 1992, ApJ, 387, 170
Fryxell, B., Olson, K., Ricker, P., et al. 2000, ApJS, 131, 273
Gent, F. A., Shukurov, A., Fletcher, A., Sarson, G. R., & Mantere, M. J. 2013, MNRAS, 432, 1396
Glover, S. 2013, in Astrophysics and Space Science Library, Vol. 396, Astrophysics and Space Science Library, ed. T. Wiklind, B. Mobasher, & V. Bromm, 103
Haugen, N. E., Brandenburg, A., & Dobler, W. 2004, Phys. Rev. E, 70, 016308
Hill, A. S., Joung, M. R., Mac Low, M.-M., et al. 2012, ApJ, 750, 104
Jacobson, M. Z. 2001, Nature, 409, 695
Kazantsev, A. P. 1968, Soviet Journal of Experimental and Theoretical Physics, 26, 1031
Krause, F., & Raedler, K.-H. 1980, Mean-field magnetohydrodynamics and dynamo theory
Latif, M. A., Schleicher, D. R. G., Schmidt, W., & Niemeyer, J. 2013, ApJ, 772, L3
Lee, D. 2013, Journal of Computational Physics, 243, 269
Lee, D., & Deane, A. E. 2009, Journal of Computational Physics, 228, 952
Miyoshi, T., & Kusano, K. 2005, Journal of Computational Physics, 208, 315
Norman, M. L., & Bryan, G. L. 1999, in Lecture Notes in Physics, Berlin Springer Verlag, Vol. 530, The Radio Galaxy Messier 87, ed. H.-J. Röser & K. Meisenheimer, 106
Pan, L., Desch, S. J., Scannapieco, E., & Timmes, F. X. 2012, ApJ, 756, 102
Pan, L., & Scalo, J. 2007, ApJ, 654, L29
Pan, L., & Scannapieco, E. 2010, ApJ, 721, 1765
—. 2011, Phys. Rev. E, 83, 045302
Pan, L., Scannapieco, E., & Scalo, J. 2011, ArXiv e-prints, arXiv:1110.0571
—. 2013, ArXiv e-prints, arXiv:1306.4663
Pichon, C., Scannapieco, E., Aracil, B., et al. 2003, ApJ, 597, L97

Pieri, M. M., Schaye, J., & Aguirre, A. 2006, ApJ, 638, 45
Pitsch, H. 2006, Annual Review of Fluid Mechanics, 38, 453
Quillen, A. C. 2002, AJ, 124, 400
Rebusco, P., Churazov, E., Böhringer, H., & Forman, W. 2005, MNRAS, 359, 1041
Ruszkowski, M., & Oh, S. P. 2010, ApJ, 713, 1332
Ruzmaikin, A. A., Sokolov, D. D., & Shukurov, A. M., eds. 1988, Astrophysics and Space Science Library, Vol. 133, Magnetic fields of galaxies
Ryu, D., Kang, H., Cho, J., & Das, S. 2008, Science, 320, 909
Ryu, D., Schleicher, D. R. G., Treumann, R. A., Tsagas, C. G., & Widrow, L. M. 2012, Space Sci. Rev., 166, 1
Sakuma, E., Ota, N., Sato, K., Sato, T., & Matsushita, K. 2011, PASJ, 63, 979
Scannapieco, E., Pichon, C., Aracil, B., et al. 2006, MNRAS, 365, 615
Scannapieco, E., Schneider, R., & Ferrara, A. 2003, ApJ, 589, 35
Schaye, J., Aguirre, A., Kim, T.-S., et al. 2003, ApJ, 596, 768
Schekochihin, A. A., Cowley, S. C., Hammett, G. W., Maron, J. L., & McWilliams, J. C. 2002, New Journal of Physics, 4, 84
Schekochihin, A. A., Cowley, S. C., Taylor, S. F., Maron, J. L., & McWilliams, J. C. 2004, ApJ, 612, 276
She, Z.-S., & Leveque, E. 1994, Physical Review Letters, 72, 336
Shraiman, B. I., & Siggia, E. D. 2000, Nature, 405, 639
Sreenivasan, K. R. 1996, Physics of Fluids, 8, 189
Sur, S., Schleicher, D. R. G., Banerjee, R., Federrath, C., & Klessen, R. S. 2010, ApJ, 721, L134
Turk, M. J., Oishi, J. S., Abel, T., & Bryan, G. L. 2012, ApJ, 745, 154
Twarog, B. A., Ashman, K. M., & Anthony-Twarog, B. J. 1997, AJ, 114, 2556
Watanabe, T., & Gotoh, T. 2004, New Journal of Physics, 6, 40